Optics Letters

On-chip dense quantum frequency comb generation via SFWM in an AlGaAs-on-insulator resonator

J. S. S. Durán Gómez,[1,2,*] Jan Heine,[1,2] Mina Abdelmeseih,[1] Alí M. Angulo M.,[1,2] Stuart May,[3] Marc Sorel,[3,4] and Michael Kues[1,2]

[1] Institute of Photonics, Leibniz University Hannover, Nienburger Str. 17, 30167 Hannover, Germany
[2] Cluster of Excellence PhoenixD (Photonic, Optics, and Engineering – Innovation Across Disciplines), Leibniz University Hannover, Hannover, Germany
[3] School of Engineering, University of Glasgow, Glasgow G12 8QQ, UK
[4] TeCIP Institute, Sant'Anna School of Advanced Studies, Via Moruzzi 1, 56127 Pisa, Italy
*samuel.gomez@iop.uni-hannover.de

Received 25 May 2026; revised 8 July 2026; accepted 14 July 2026; posted 14 July 2026; published 31 July 2026

Bright and broadband integrated photon sources at telecom wavelengths are essential for quantum communication and information processing. Materials with high nonlinear refractive index (n_2), such as aluminum gallium arsenide (AlGaAs), enable efficient nonlinear interactions at low excitation powers in integrated cavities. Here, we demonstrate a broadband quantum frequency comb (QFC) in a low free spectral range (FSR) (45 GHz) aluminum gallium arsenide on insulator (AlGaAsOI) resonator, with up to 40 pairwise frequency-correlated modes across a 1.97 THz bandwidth in the C-band. The dense mode spacing enables scalable frequency multiplexing and frequency-bin encoding within a compact device operating at a low excitation power of 6.33 μW. The measured joint-spectral intensity (JSI) is well reproduced by a theoretical model, enabling predictive control of spectral correlations across the generated QFC. The moderate Q-factor provides a tradeoff between nonlinear enhancement, broadband phase-matching, and number of accessible modes, supporting dense multimode operation over a large spectral range. These results highlight the potential of AlGaAsOI resonators for scalable low-power QFC sources.

https://doi.org/10.1364/OL.605643

The development of photonic integrated circuits on highly nonlinear, low-loss material platforms compatible with CMOS fabrication is driving advances in photonic applications such as optical signal processing, multi-wavelength lasers, metrology, spectroscopy, and quantum information science [1,2]. In particular, bright integrated photon sources are key elements for enabling photonic quantum applications. Many materials have been explored for use as quantum light sources such as silicon dioxide (SiO_2) [3], silicon on-insulator (SOI) [4,5], silicon nitride (Si_3N_4) [6–8], gallium nitride (GaN) [9] and AlGaAs [2,10,11], among others. AlGaAsOI has shown favorable applications such as efficient frequency comb generation [12–15], second harmonic generation [16], four-wave mixing [17,18], supercontinuum generation [19], and photon pair generation through spontaneous second- [20] and third-order parametric processes [2,10,11,21].

Generation of correlated photonic quantum states can be achieved either via spontaneous parametric down-conversion (SPDC) due to the strong second-order nonlinearity ($\chi^{(2)}$), or spontaneous four-wave mixing (SFWM) through the third-order nonlinearity ($\chi^{(3)}$) present in the AlGaAs platform [2,21]. In particular, for SFWM process, two pump photons are annihilated, creating a pair of signal and idler photons with an energy signature of $2\omega_p = \omega_s + \omega_i$, where the subscripts p, s and i label the pump, signal, and idler photons, respectively. In practice, SFWM generates photon pairs close to the pump frequency, making filtering more challenging.

AlGaAs exhibits attractive properties for the deployment of integrated photon sources, such as a high refractive index (n ≈ 3.4), bandgap tunability through variations of the aluminum concentration, and high $\chi^{(3)}$, which is almost 4 times higher than SOI and 100 times higher than Si_3N_4. These features make it a promising platform for scalable nonlinear photonic devices [2,22]. In addition to its high non-linear refractive index, alternative configurations, such as integrated cavities, are often used to enhance the photon pair generation rates and to tailor the continuous bi-photon emission from SFWM into discrete narrow resonances to produce frequency-correlated modes, as shown in Fig. 1(a) [7,10]. The resulting QFC consists of multiple pairwise frequency-correlated signal-idler mode pairs distributed across the discrete cavity resonances. The discrete resonances supported by such cavities allow frequency-bin manipulation of the photonic states (e.g., via electro-optic mixing), which can be exploited for quantum optical algorithms and sensing applications [23]. Previous AlGaAs platforms have demonstrated very high pair generation efficiency (PGE) for individual signal–idler mode pairs and multiplexed configurations [8,24]. Since the number of generated photons scales as $N_{s,i} \propto Q^3/L^2$ [10], high efficiencies are typically achieved with high-Q and short cavities. However, as the cavity linewidth decreases with

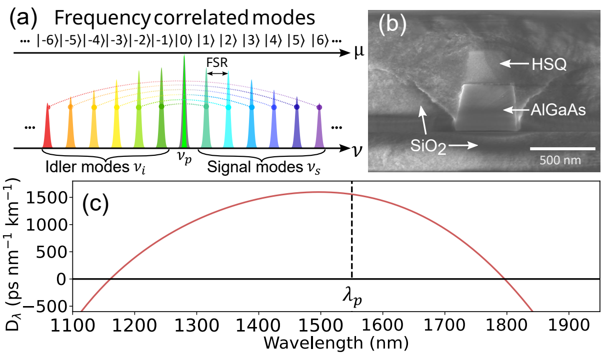

Fig. 1. (a) Schematic representation of the SFWM process illustrating the symmetric generation of quantum frequency-correlated modes around the pump frequency. (b) SEM image of the cross-section of the waveguide with HSQ on-top cladding and SiO_2 boxing. (c) Simulated dispersion for the TM_{00} mode.

increasing Q-factor, integrated dispersion progressively shifts the resonances away from the optimal phase-matching frequencies. As a result, the overlap between the cavity resonances and the SFWM gain bandwidth is reduced for modes farther from the pump, limiting the usable bandwidth for broadband multimode generation.

In this work, we demonstrate a broadband QFC in an AlGaAs resonator via SFWM. The low-FSR (45 GHz) enables dense frequency multiplexing with up to 40 measured frequency-correlated mode pairs across a 1.97 THz bandwidth in the C-band while operating at a low pump power of 6.33 μW. The moderate cavity Q-factor provides a trade-off between nonlinear enhancement and broadband multimode operation, enabling dense frequency multiplexing with a large number of frequency-correlated modes. Furthermore, the excellent agreement between the measured and theoretical JSI enables predictive control of the generated spectral correlations across the QFC.

In Fig. 1(b), an SEM image of the tip of the AlGaAsOI waveguide is shown. The $Al_xGa_{1-x}As$ sample was fabricated with an aluminum concentration of x = 0.25 and hydrogen silsesquioxane (HSQ) top-cladding (details on the fabrication are described in [16]). The photon source consists of an integrated racetrack resonator coupled to a single bus waveguide, with a cross section of 700 nm wide and 340 nm thick for both the resonator and the bus waveguide. Inverse tapers were used to optimize the coupling to the chip for the vertical polarization. Simulations were performed to determine the effective refractive index for the TM_{00} mode. We considered the cross section of the ridge waveguide embedded in SiO_2, given that the refractive index of HSQ is similar to that of SiO_2 [12]. The refractive index of AlGaAs was estimated in terms of the concentration of aluminum [25], while the Sellmeier equation was used to obtain the refractive index of SiO_2. The dispersion was obtained through the equation $D_\lambda = -\frac{\lambda}{c}\frac{d^2 n_{\text{eff}}(\lambda)}{d\lambda^2}$, resulting in an anomalous dispersion at 1550 nm (shown in Fig. 1(c)). Furthermore, the cavity length is $L = 1602.42$μm, which results in a 45 GHz FSR. The resonator and bus waveguide were separated by 250 nm with an interaction length of 5 μm. We characterized the cavity using a high-resolution spectrometer (WaveAnalyzer 1500 s), as shown in Fig. 2(a). Figure 2(b) shows an SEM image of the fabricated racetrack resonator. A Lorentzian fit of the transmission spectrum yielded a 4.32 GHz (FWHM) resonance bandwidth, corresponding to an average Q-factor of 44800 (Fig. 2(c)). Moreover, the FSR is not constant due to dispersion. This variation can be quantified through the integrated dispersion, defined as the deviation of the actual resonant frequencies from an ideal equidistant frequency grid centered at the excitation frequency. By analyzing this parameter, we characterized how the resonance frequencies shift relative to the pump resonance, as described by Eq. (1):

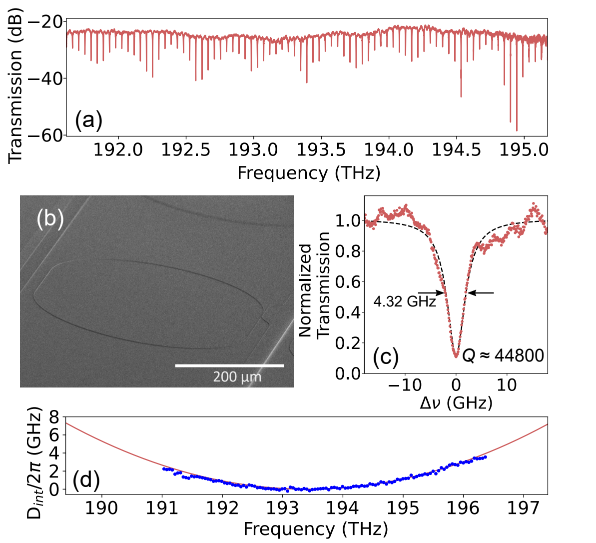

Fig. 2. (a) Normalized transmission around the excitation frequency. (b) SEM image of the AlGaAsOI racetrack resonator. (c) Measured and fitted normalized transmission of the pump resonance centered at 193.4 THz. (d) Simulated (red curve) and experimental data (blue dots) integrated dispersion. Error bars are smaller than the marker size.

$$D_{int}(\mu) = \omega_\mu - \omega_0 - \mu D_1, \tag{1}$$

where μ denotes the relative mode index, ω_μ the resonant frequencies, and $D_1/2\pi$ corresponds to the FSR at the pump frequency. Hence, the resonant frequencies can be predicted theoretically through $\omega_l = \frac{2\pi l c}{L n_{\text{eff}}}$, with l as the azimuthal mode number and c as the speed of light. The azimuthal mode number and the relative mode index are related by $\mu = l - l_p$ (l_p, as the azimuthal mode for the excitation field). Resonant frequencies were extracted from the measured spectra. The extracted integrated dispersion agrees well with the theoretical model and exhibits a weak parabolic dependence (with $D_{int} > 0$ corresponding to anomalous dispersion). The maximum deviation remains below 4 GHz over the relevant spectral range, thereby fulfilling the phase-matching condition for SFWM (see Fig. 2(d)).

Frequency-correlated photon pairs were measured with the experimental setup shown in Fig. 3. A fiber-coupled continuous-wave (CW) laser (Cobrite laser), centered at 193.4 THz, is polarization-filtered using a slow-axis polarizer. Spectral out-of-band noise is suppressed by a DWDM filter centered at the laser frequency (ITU-channel C34) with 100 GHz bandwidth (1.5 dB insertion loss (IL)). The excitation is coupled to the AlGaAsOI chip via polarization-maintaining lensed fibers (2.5 μm spot size), matched to inverse-tapered couplers. The measured fiber-to-fiber IL is 26 dB (13 dB per facet, assuming symmetric coupling). The lensed fiber is aligned to provide vertical polarization, which excites the fundamental TM_{00} mode of the

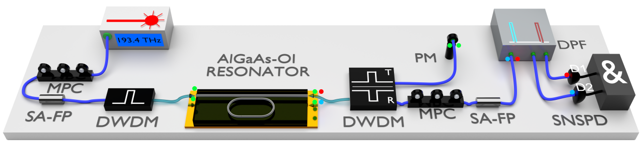

Fig. 3. Schematic representation of the experimental setup employed for the QFC generation. The green spheres denote the pump, while the blue and red spheres denote the signal and idler photons, respectively. Manual polarization controller (MPC), slow-axis fiber polarizer (SA-FP), dense wavelength division multiplexing (DWDM), digital programmable filter (DPF), superconducting nanowire single-photon detector (SNSPD), power meter (PM).

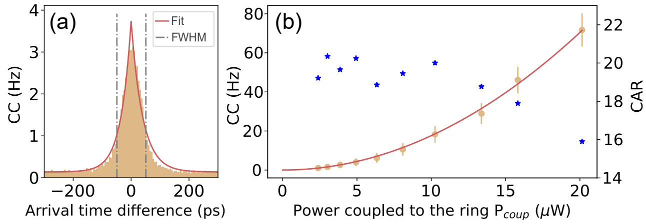

Fig. 4. (a) Coincidence histogram for an on-chip power of 15.82 μW fitted to a Lorentzian function to determine the coincidence counts at FWHM. (b) Coincidence counts and CAR as a function of the on-chip pump power.

micro-resonator. To optimize the power coupled to the resonator, the cavity resonance is aligned to the excitation field frequency in combination with a temperature controller. The generated frequency-correlated photon pairs are coupled out along with the residual excitation field and separated using a second C34 DWDM filter with 200 GHz bandwidth. The residual light is used to monitor the coupling of the excitation field to the resonance with a power meter while the signal and idler photons, generated in the fundamental TM_{00} mode, are polarization-filtered with a second SA-FP. This filtering suppresses uncorrelated single-photon noise, generated in the orthogonal mode (TE mode). The signal and idler photons are then spectrally demultiplexed using a DPF (Waveshaper 4000 s with 4.5 dB loss) according to their optical frequencies rather than their polarization. Finally, the two frequency channels are directed to two SNSPDs (0.46 dB) and their arrival-time differences are recorded with a time-to-digital converter (Swabian Instruments TimeTagger Ultra). To characterize the PGE of our integrated photon source, coincidence counts were measured as a function of power. The generation rate of correlated photons via SFWM exhibits quadratic polynomial dependence on the excitation power, characteristic of energy-time entangled photon-pair generation. It can be isolated through heralded detection, as described in [11], with $N_{s,i} = aP^2$, where a represents the PGE. The overall generation efficiency was assessed using a 1.5 THz filter covering cavity modes 5 to 38 . Each symmetric mode pair ($\pm\mu$) defines a signal–idler pair, yielding 33 correlated pairs. Histograms were acquired for 360 s with a 5 ps binwidth, and coincidences were postselected using the full width at half maximum (FWHM) of the coincidence histogram, as shown in Fig. 4(a) (error bars denote one standard deviation). The coincidence-to-accidental ratio (CAR) was calculated as $CAR = \frac{CC}{AC} - 1$, where CC is the integrated coincidence counts, and AC is the average accidental counts estimated from the histogram background over an equivalent coincidence window. No accidental counts were subtracted. The results were fitted for different excitation powers to extract the efficiency, as shown in Fig. 4(b). The coincidence rate exhibits the expected quadratic behavior, yielding a detected efficiency of $a = 0.176 \times 10^{12}$ pairs/(s·W^2) in the 1.5 THz bandwidth, with a CAR greater than 15 for all excitation powers considered. To quantify the system performance, we evaluate the losses along the detection path. The total losses from the bus waveguide to the detectors are 20.57 dB and 20.83 dB for the signal and idler channels, respectively, corresponding to detection efficiencies of $\eta_s = 8.77 \times 10^{-3}$ and $\eta_i = 8.26 \times 10^{-3}$, and a pair detection probability of $\eta_{\text{pair}} = \eta_s \eta_i = 7.24 \times 10^{-5}$ (0.0072%). Accounting for these losses, we estimate an on-chip PGE of $a_{\text{on-chip}} \approx (6.1 \pm 1.6) \times 10^{12}$ pairs/(s·W^2), assuming a conservative uncertainty of 1 dB in the total measured insertion loss [11]. The dominant limitation is fiber-to-chip coupling, which is not intrinsic to the AlGaAsOI platform and can be mitigated through optimized inverse-taper designs, improved mode converters, better facet preparation, anti-reflection coatings, and improved packaging [8,24,26]. Previous works have demonstrated coupling losses approaching ~3 dB per facet in optimized AlGaAsOI devices. A quantitative comparison with representative SFWM photon-pair sources is provided in Table S1 in Supplement 1, highlighting key architectural parameters for broadband frequency-multiplexed operation.

Finally, using the effective refractive index of the TM_{00} mode and the cavity length, the JSI was simulated to estimate the spectral bandwidth of the SFWM process in the cavity along the main diagonal, which is described by [7]:

$$|G_{cav}(\mu)|^2 = \zeta_{-\mu}\zeta_{\mu} \int_{-\infty}^{\infty} d\omega_p \, \alpha(\omega_p) \times \int_{-\infty}^{\infty} d\omega \, A_{\mu}^2(\omega) A_{-\mu}^2(2\omega_p - \omega) sinc^2\left(\frac{L\Delta\beta}{2}\right), \quad (2)$$

where μ is the relative mode index, $\Delta\beta = 2\beta_p(\omega_p) - \beta_s(\omega) - \beta_i(2\omega_p - \omega)$ is the phase matching condition with β as the propagation constant and $\zeta_{-\mu}, \zeta_{\mu}$ are constants of the cavity modes; $\alpha(\omega_p)$ is the pump envelope function and $A_{\mu}^2(\omega)$ is the Airy function that describes the cavity effect as [3]:

$$A_{\mu}^2(\omega_{\mu}) = \left| \frac{t_{\mu}}{1 - r_{\mu} e^{i\beta_{\mu}(\omega_{\mu})L}} \right|^2, \quad (3)$$

where t_{μ} and r_{μ} denote the transmissivity and reflectivity amplitudes of the cavity and, the Q-factor is related to the reflectivity as $|r_{\mu}| = 1 - \frac{l\pi}{Q}$. The pump envelope was modeled as a Gaussian function with a linewidth of $\delta\nu_p = 100$ kHz, obtained from the data specifications of the CW laser. The main diagonal was calculated for 66 modes and for a straight waveguide, which allows us to compare the bandwidth with and without the cavity. Subsequently, frequency-correlated mode pairs were measured using 20 GHz rectangular filters, selected with the programmable filter around the center frequency of each resonance, using an excitation power of 6.33 μW. Although the resonator supports 44 modes, those close to the pump ($|\mu| \leq 4$) are suppressed by the output DWDM filter, resulting in 40 experimentally accessible modes. Coincidence counts and CAR were extracted from arrival time histograms for each mode (Fig. 5(a)). Broadband measurements yield CAR values of approximately 20 due to the simultaneous collection of multiple frequency-correlated mode pairs within the 1.5 THz spectral window, whereas individual

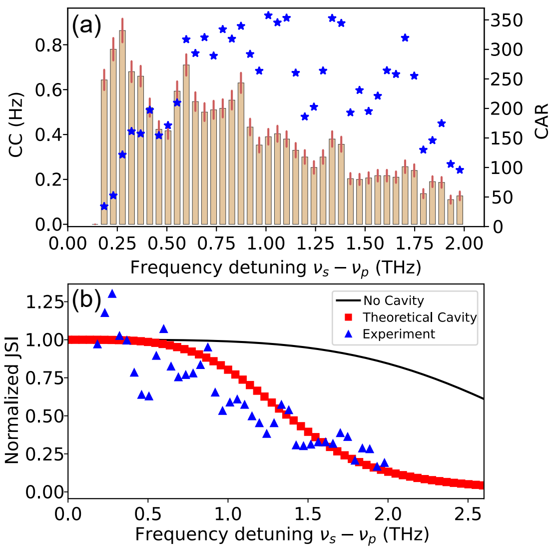

Fig. 5. (a) Coincidence counts and CAR as functions of frequency detuning for 40 different modes covering approximately 2 THz bandwidth. (b) Normalized JSI comparing theory and experiment for the cavity and a straight waveguide.

mode pairs measured with narrowband filtering reach CAR values up to 350. Lastly, we compare the measured JSI with the theoretical model by fitting the 40 frequency-correlated modes. The experimental and theoretical JSIs were normalized to the peak amplitude of the fitted experimental JSI, allowing a direct comparison of their spectral distributions independently of the absolute coincidence rate. The simulated JSI further predicts limited unfiltered heralded spectral purity under CW pumping; however, significantly higher purity is expected for pump bandwidths comparable to the cavity linewidth (see Supplement 1). Figure 5(b) shows excellent agreement, demonstrating bandwidth reduction due to cavity and dispersion effects and confirming predictive control over the spectral correlations. The overall performance of the source is determined by a trade-off between the number of accessible frequency modes, IL, and PGE. In the present device, the reduced FSR enables up to 40 frequency-correlated modes. Although the current implementation is limited by fiber-to-chip coupling losses, these are not intrinsic to the AlGaAsOI platform. Furthermore, this design prioritizes channel density over maximum brightness while enabling predictive control of the generated spectral correlations, making it particularly attractive for frequency-multiplexed quantum photonic architectures.

In conclusion, we demonstrate broadband bi-photon frequency correlations with 45 GHz spacing, compatible with DWDM grids, in an AlGaAsOI racetrack resonator operating in the C-band. The device supports up to 40 frequency-correlated mode pairs across a 1.97 THz bandwidth, enabled by a small FSR that allows dense frequency multiplexing and scalable frequency-bin encoding. The measured results are well reproduced by a theoretical model of the JSI, demonstrating predictive control of spectral correlations across the generated QFC. The moderate cavity Q-factor provides a tradeoff between nonlinear enhancement, broadband phase matching, and accessible mode number, enabling dense multimode operation across a large spectral range. The main limitation is fiber-to-chip coupling loss, which is not intrinsic to the platform and can be mitigated through improved coupling schemes. These results highlight the potential of AlGaAsOI integrated resonators for scalable low-power, broadband multimode quantum light sources and quantum photonic systems.

Funding. Deutsche Forschu ngsgemeinschaft (PhoenixD EXC2122, Project ID: 390833453); European Research Council (947603, QFreC Project); Engineering and Physical Sciences Research Council (EP/X012689/1); Bundesministerium für Forschung, Technologie und Raumfahrt (InQL project).

Disclosures. The authors declare no conflict of interest.

Data availability. The data that support this study are available from the corresponding author upon reasonable request.

Supplemental document. See Supplement 1 for supporting content.

REFERENCES

1. L. Minhao Pu, E. Ottaviano, H. Semenova, *et al.*, in *Progress in Electromagnetic Research Symposium (PIERS)* (2016), p. 3160.
2. T. J. Steiner, M. Shen, J. E. Castro, *et al.*, Opt. Quantum **1**, 55 (2023).
3. E. Ortiz-Ricardo, C. Bertoni-Ocampo, M. Maldonado-Terrón, *et al.*, Photonics Res. **9**, 2237 (2021).
4. R. Wakabayashi, M. Fujiwara, K.-i. Yoshino, *et al.*, Opt. Express **23**, 1103 (2015).
5. A. M. Angulo, J. Heine, J. D. Gomez, *et al.*, Opt. Lett. **48**, 5583 (2023).
6. W. Wen, W. Yan, C. Lu, *et al.*, Phys. Rev. Appl. **20**, 064032 (2023).
7. Z. Yin, K. Sugiura, H. Takashima, *et al.*, Opt. Express **29**, 4821 (2021).
8. R. Chen, Y.-H. Luo, J. Long, *et al.*, Phys. Rev. Lett. **133**, 083803 (2024).
9. H. Zeng, Z.-Q. He, Y.-R. Fan, *et al.*, Phys. Rev. Lett. **132**, 133603 (2024).
10. T. J. Steiner, J. E. Castro, L. Chang, *et al.*, PRX Quantum **2**, 010337 (2021).
11. H. Mahmudlu, S. May, A. Angulo, *et al.*, Opt. Lett. **46**, 1061 (2021).
12. M. Pu, L. Ottaviano, E. Semenova, *et al.*, Optica **3**, 823 (2016).
13. L. Chang, W. Xie, H. Shu, *et al.*, Nat. Commun. **11**, 1331 (2020).
14. H. Hu, F. Da Ros, M. Pu, *et al.*, Nat. Photonics **12**, 469 (2018).
15. L. Ottaviano, M. Pu, E. Semenova, *et al.*, Opt. Lett. **41**, 3996 (2016).
16. S. May, M. Kues, M. Clerici, *et al.*, Opt. Lett. **44**, 1339 (2019).
17. D. H. Espinosa, K. M. Awan, M. Odungide, *et al.*, Opt. Commun. **479**, 126450 (2021).
18. J. S. Aitchison, K. Dolgaleva, L. Qian, *et al.*, Opt. Lett. **35**, 4093 (2010).
19. S. May, M. Clerici, and M. Sorel, Sci. Rep. **11**, 2052 (2021).
20. J. E. Sipe and Z. Yang, Opt. Lett. **32**, 3296 (2007).
21. G. Maltese, M. I. Amanti, F. Appas, *et al.*, NPJ Quantum Inform. **6**, 1 (2020).
22. H. Wang, Q. Zeng, H. Ma, *et al.*, Adv. Devices Instrum. **5**, 0032 (2024).
23. Y. Wang, Z. Hu, B. C. Sanders, *et al.*, Front. Phys. **8**, 479 (2020).
24. Y. Pang, J. E. Castro, T. J. Steiner, *et al.*, PRX Quantum **6**, 010338 (2025).
25. S. Adachi, J. Appl. Phys. **58**, R1 (1985).
26. J. E. Castro, T. J. Steiner, L. Thiel, *et al.*, APL Photon. **7**, 096103 (2022).